Sheet Metal Forming Springback Prediction Using Image Geometrics (SPIG): A Novel Approach Using Heatmaps and Convolutional Neural Network

Du Chen[1], Mariluz Penalva Oscoz[2], Yang Hai[3], Martin Rebe Ander[2], Frans Coenen[1] and Anh Nguyen[1]

[1]*Department of Computer Science, The University of Liverpool, Liverpool, L693BX, U.K.*

[2]*TECNALIA, Basque Research and Technology Alliance, Sebastian, Spain*

[3]*Nanjing EITRI, Nanjing, China*

Keywords: Single Point Incremental Forming, Springback Prediction, Image Geometries, Deep Learning, Convolutional Neural Network.

Abstract: We propose the Springback Prediction Using Image Geometrics (SPIG) approach to predict springback errors in Single Point Incremental Forming (SPIF). We achieved highly accurate predictions by converting local geometric information into heatmaps and employing ResNet based method. Augmenting the dataset twenty-four-fold through various transformations, our ResNet model significantly outperformed LSTM, SVM, and GRU alternatives in terms of the MSE and RMSE values obtained. The best performance result in an R^2 value of 0.9688, 4.95% improvement over alternative methods. The research demonstrates the potential of ResNet models in predicting springback errors, offering advancements over alternative methods. Future work will focus on further optimisation, advanced data augmentation, and applying the method to other forming processes. Our code and models are available at https://github.com/DarrenChen0923/SPIF.

1 INTRODUCTION

Single Point Incremental Forming (SPIF)(Martins et al., 2008) is an advanced sheet metal cold forming technique that uses a Computer Numerical Control (CNC) machine to manufactured desired shapes. The alternative is hot forming where the material to be fabricated is first heated up. Cold forming does not require this. Therefore, cold forming is more cost-effective and eco-friendly than hot forming. The disadvantage of SPIF cold forming is that the process features springback, a property of metals where the material tries to return to its original shape after bending. This means that the manufactured shape is different from the specified shape CAD. This is illustrated in the Figure 1, which shows a flat-topped pyramid shape. The solid line is the pre-specified CAD shape, while the dashed line is the final shape. An inspection of the figure shows that the two shapes are not the same. Therefore Springback errors can cause deviations between the final formed part and the intended shape, which is particularly important in fields such as aerospace manufacturing where extremely high part accuracy is required. Geometric accuracy in the SPIF process remains a major challenge due to the springback effect.

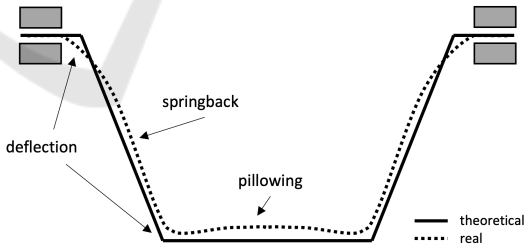

Figure 1: Illustration of the springback effect when conducting cold sheet metal forming.

Path correction and springback error prediction methods have evolved with the advent of artificial intelligence, particularly deep learning, enhancing accuracy. For example, Artificial Neural Networks (ANNs), regression, and other AI techniques have all been considered effective solutions (Bahloul et al., 2013; Spathopoulos and Stavroulakis, 2020; Zwierzycki et al., 2017). The challenge is how to define the training data required for various AI learners to effectively represent local geometries so that

Chen, D., Oscoz, M. P., Hai, Y., Ander, M. R., Coenen, F. and Nguyen, A.
Sheet Metal Forming Springback Prediction Using Image Geometrics (SPIG): A Novel Approach Using Heatmaps and Convolutional Neural Network.
DOI: 10.5220/0013673100004000

In *Proceedings of the 17th International Joint Conference on Knowledge Discovery, Knowledge Engineering and Knowledge Management (IC3K 2025) - Volume 1: KDIR*, pages 28-38

the springback of previously unseen parts can be predicted. Muhamad *et al.*(Khan et al., 2015), writing in 2015, propose a strategy to represent local geometry as a series of points. The goal is to create a set of local geometries that are a superset of all possible local geometries of any part we may wish to manufacture. The work introduced in (Khan et al., 2015) used *k*-Nearest Neighbour (*k*NN) classification, a mature machine learning classification technique, and proved that the proposed method worked well. Du Chen *et al.* (Chen et al., 2023) proposed a method based on GRU (Gated Recurrent Unit) and data augmentation technology that significantly expanded the dataset size through data augmentation and used the GRU model to predict springback error, achieving excellent results. Their research showed that by representing local geometry as a point sequence and combining it with deep learning, the accuracy of springback error prediction can be effectively improved.

However, the above methods have shortcomings when expressing local geometric information and processing complex geometric relationships, limiting further improvement in prediction accuracy. The Local Geometry Matrix (LGM) and Local Distance Metric (LDM) methods proposed in (El-Salhi et al., 2012; El-Salhi et al., 2013), although they have improved the accuracy of geometric representation to a certain extent, still had limitations in processing complex geometric shapes. Moreover, existing methods mostly used LSTM models. Although they perform well in processing sequence data, their structure entails a computational overhead.

Building on previous research, we propose the springback prediction using the Image Geometrics (SPIF) approach to springback prediction. An approach that features three novel elements: firstly a new local geometry expression method using heatmaps to capture the geometric information of local areas. A method that can more intuitively and accurately represent local geometric features. Second, we convert the local geometry problem into an image processing problem and use a few residual blocks to process heatmaps, improving prediction accuracy and robustness. Thirdly the use of a ResNet Model. Experiments demonstrated the superior performance of the ResNet model in springback error prediction, significantly better than all previous methods. The experimental results reported later in this paper show that this new method achieves better results, with a best $R2$ value of 0.9688 compared to the previous best $R2$ value of 0.9228 (Chen et al., 2023), an increase of 4.95%.

To summarize the above, our contributions are as follows:

1. The use of heatmaps to capture local geometric details accurately.
2. Converting the local geometry problem into an image-processing task for better prediction.
3. Demonstrating ResNet's superior performance over previous methods in springback prediction.

The rest of this paper is organized as follows: Section 2 presents the related work underpinning the work presented. Section 3 introduces the method in detail, including presenting the proposed SPIG approach, problem transformation, and the ResNet model. The experimental design and results are presented and discussed in Section 4. The paper is concluded in Section 5 with a summary of the main contributions of this paper and proposes future research directions.

2 RELATED WORK

In the SPIF process, predicting springback error has been a significant research direction. Various regression methods have been employed to model and predict these errors. For instance, multiple linear regression (Tranmer and Elliot, 2008), regression trees (Loh, 2011), Support Vector Machines (SVM) (Boser et al., 1992), and Gaussian processes (Seeger, 2004) are common approaches (Bahloul et al., 2013). Additionally, genetic algorithms (Holland, 1975) combined with finite element simulations (Belytschko and Hodge Jr, 1970) have been used to optimize moulding parameters and reduce springback error (Maji and Kumar, 2020). However, these traditional methods often struggle with complex geometric relationships.

Deep learning has recently been applied to springback error prediction. For instance, a GRU-based method combined with data augmentation significantly expanded the dataset and achieved excellent results (Chen et al., 2023). The LSTM model captures time correlations of springback errors, improving prediction accuracy (Bingqian et al., 2024). Other studies have integrated finite element simulation with machine learning to optimize forming parameters and sheet shapes, thus reducing springback (Sbayti et al., 2020; Spathopoulos and Stavroulakis, 2020). Notably, combining finite element simulation with neural network-based optimization has proven effective (Spathopoulos and Stavroulakis, 2020).

Representing local geometric information is crucial in springback error prediction. Traditional methods often rely on point sequences (El-Salhi et al., 2012), while the local geometry matrix (LGM) and local distance metric (LDM) methods use grids to rep-

resent geometric shapes (El-Salhi et al., 2012; El-Salhi et al., 2013). Point sequence methods typically employ k-nearest neighbour (kNN) (Fix, 1985) and dynamic time warping (DTW) (Sakoe and Chiba, 2003) for classification (Khan et al., 2012; Khan et al., 2015). Despite improvements in geometric representation accuracy, these methods struggle with complex geometric changes, limiting their predictive accuracy. Recent approaches have integrated sophisticated techniques like machine learning and finite element simulations to enhance prediction accuracy, aiming to capture more intricate geometric details and complex relationships in forming processes.

Image processing techniques, especially convolutional neural networks (CNN) (LeCun et al., 2002), excel at capturing complex geometric relationships. CNNs automatically extract features from images and perform efficient learning through deep network structures. Other notable techniques include edge detection methods like the Canny edge detector (Canny, 2009), the Scale-Invariant Feature Transform (SIFT) (Lowe, 2004), and the Hough transform (Duda and Hart, 1972) for detecting shapes. Morphological image processing techniques (Serra, 1983), such as dilation and erosion, provide support for shape analysis and noise removal. The Harris corner detector (Harris et al., 1988) identifies key points in images. Generative models like Generative Adversarial Networks (GANs) (Goodfellow et al., 2014) and Variational Autoencoders (VAEs) (Kingma et al., 2013) have been used for data augmentation by adding realistic noise, enhancing training datasets and improving model robustness.

Integrating recent high-quality studies contextualizes our contributions within the broader landscape of springback prediction research. For instance, a Simulated Annealing Particle Swarm Optimization (SAPSO) optimized Support Vector Regression (SVR) algorithm has been proposed for high-accuracy springback prediction, demonstrating the application of machine learning in bending processes (He et al., 2025). A springback prediction model for DP780 steel using a modified Yoshida-Uemori two-surface hardening model has been shown to significantly enhances prediction accuracy (Zajkani and Hajbarati, 2017). Optimized constitutive equations in TRIP1180 steel cold stamping also show substantial improvements in prediction accuracy (Seo et al., 2017). Additionally, a springback prediction model for multi-cycle bending, validated through extensive experimental data, has been developed based on different hardening models (Zajkani and Hajbarati, 2017). An anisotropic hardening model for high-strength steel has also been introduced, demonstrating effectiveness in both numerical and experimental studies (Zeng and Xia, 2005). These studies highlight the importance of advanced optimization algorithms and refined material models in enhancing springback prediction accuracy.

In our research, we convert local geometric information into heatmaps and utilize the ResNet model for processing (He et al., 2016). This approach significantly improves springback error prediction, outperforming previous methods. Leveraging CNNs for detailed geometric information provides robust and accurate predictions. Transforming the problem into an image-processing task enhances feature extraction capabilities, leading to superior accuracy and stability. Additionally, data augmentation techniques like rotation, flipping, scaling, and translation expand the dataset, further improving model robustness.

3 METHODOLOGY

3.1 The Springback Prediction Using the Image Geometries (SPIG)

The core component of the proposed Springback Prediction using Image Geometries (SPIG) approach is generating the required local geometry images. The proposed process is discussed in Sub-section 3.1.2. The resulting image set $D = \{I_1, I_2, \dots\}$ is then the input to a prediction model to produce springback predictions for the item to be manufactured, which can then be applied in reverse to the CAD definition to produce a corrected definition. The calculation of springback error values corresponding to the images is described in Sub-section 3.1.1.

Algorithm 1 presents the overall process of sprinback error calculation. To accommodate multiple scales of local features with different grid sizes, the entire heatmap is divided into $w \times w$ sub-images, where $w/3$ can be 5mm, 10mm, 15mm, or 20mm. Therefore, the sub-images sizes become 15×15 mm, 30×30 mm, 45×45 mm, and 60×60 mm, respectively. Changing these grid sizes allows the algorithm to capture local geometry, intensity distribution, or other relevant properties at different resolution levels.

3.1.1 Springback Error Calculation

The springback calculation Algorithm 1, computes the springback error for each point in the input grid set by measuring the distance between each input grid point and its corresponding point in the output grid set, as outlined in (El-Salhi et al., 2012; Gill et al., 2021; Salomon, 2006). The algorithm takes two sets

Algorithm 1: Calculate Springback Error.

Input: G_{in} (input grid), G_{out} (output grid)
Output: E (set of springback errors)
$E \leftarrow \{\}$;
for *each* g_i *in* G_{in} **do**
  $plane\_g_i \leftarrow \text{FitPlane}(g_i, G_{in})$;
  $intersect\_point \leftarrow \text{FindIntersection}(g_i, G_{out})$;
  if *intersect_point found* **then**
    $s_i \leftarrow \text{Distance}(g_i, intersect\_point)$;
    $E \leftarrow E \cup \{s_i\}$;
  else
    $E \leftarrow E \cup \{0\}$;
return E;
Function `FitPlane`(g, G)**:**
  Fit a plane to the grid point g and its neighbours in grid G *plane*
  return *plane*
Function `FindIntersection`(g_i, G_{out})**:**
  for *each* g_o *in* G_{out} **do**
    $plane\_g_o \leftarrow \text{FitPlane}(g_o, G_{out})$
    $intersect\_point \leftarrow$ CalculateIntersection$(g_i, plane g_o)$
    if *intersect_point found* **then**
      return *intersect_point*
  return null
Function `CalculateIntersection`$(point, plane)$**:**
  Calculate the intersection point of a normal from *point* with the *plane intersect_point*
  return *intersect_point*
Function `Distance`$(point_1, point_2)$**:**
  Calculate the Euclidean distance between two points *distance*
  return *distance*

of grid points, G_{in} (input grid points) and G_{out} (output grid points), and produces a set E containing the springback errors.

The algorithm initializes an empty error set E to store the calculated errors for each grid point. It iterates through each grid point g_i in the input grid G_{in}. For each point, it fits a plane to g_i and its neighbouring points in G_{in} using the *FitPlane* function to establish a local reference plane. The algorithm then determines the intersection point of the normal from g_i with the plane defined by G_{out} using the *FindIntersection* function. If an intersection point is found, it calculates the distance s_i between the intersection point and g_i using the *Distance* function. This distance, representing the springback error for that grid point, is added to E. If no intersection point is found, a value of 0 is added to E. Finally, the algorithm returns the set E, containing the springback errors for all input grid points, providing a comprehensive measure of deviations across the entire grid. Several helper functions have been included to ensure efficiency and accuracy: *FitPlane*, *FindIntersection*, *CalculateIntersection*, and *Distance*. *FitPlane* fits a plane to a grid point and its neighbours; *FindIntersection* finds the intersection of a normal with G_{out} 's plane; and *Distance* calculates the Euclidean distance between two points.

In summary, the springback calculation algorithm accurately computes the springback error for each input grid point, generating a set of errors that can be used to train a springback prediction model.

3.1.2 Local Geometry Image Generation

As noted in the introduction to this section, using images to represent local geometry is central to the proposed SPIG approach. The choice of heatmaps as a representation for local geometric information is driven by their ability to encode spatial relationships effectively. Convolutional Neural Networks (CNNs) can then be used to extract hierarchical spatial features. This approach avoids the need for extensive feature engineering and naturally integrates with ResNet's architecture, enhancing both accuracy and computational efficiency. Additionally, the heatmap format facilitates advanced data augmentation techniques, such as rotation and flipping, which improve model robustness and generalization.

The process of extract sub-images involves two key steps. First, a heatmap H is generated with reference values corresponding to the z values in the F_{in} point cloud. This heatmap visualizes the surface characteristics and variations of the input data by mapping the z values to colour intensities, creating a detailed and intuitive representation of local geometrical features. Next, a set of sub-images is extracted from the heatmap H using a sliding window technique with a predefined window size w. This method systematically captures various portions of the heatmap, resulting in a comprehensive set of local geometry images $D = \{I_1, I_2, \dots\}$. Each sub-image encapsulates specific local geometrical details, allowing the model to analyze and predict springback errors with greater precision. By focusing on localized sections of the heatmap, the SPIG approach ensures that subtle variations in geometry are accounted for, enhancing the model's accuracy and robustness.

Figure 2 illustrates the heatmap generation and processing for springback error prediction. Figure 2 features a heatmap, generated from a flat-topped pyramid shape that uses a white-to-red colour gradient to represent z values, with white indicating smaller values and red indicating larger values. The raw heatmap H shows the z values of the pyramid shape. This heatmap is then divided into $w \times w$ sub-images, which serve as inputs for the springback prediction model,

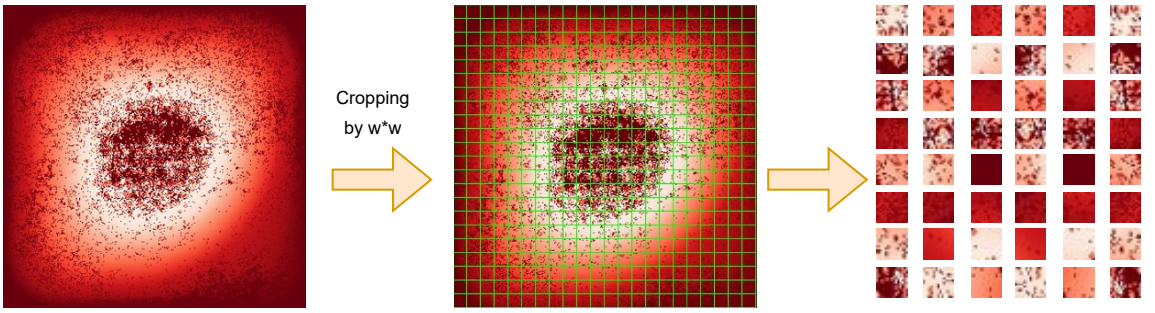

(a) Raw Heatmap H showing the z values of the flat-topped pyramid shape

(b) Heatmap H divided into w*w sub-images for input inot the prediction model

(c) Randomly sample a few sub-image examples from the sub-image dataset

Figure 2: Example of a heatmap: (a) Raw heatmap H illustrating z values using a red-to-white scale; (b) Heatmap H divided into $w \times w$ sub-images for springback prediction input.

capturing local geometric features. Randomly sampled sub-images from the dataset were used for model training and validation, highlighting the importance of each step in accurately predicting springback errors.

3.1.3 Training Set Generation

The springback calculation algorithm is designed to compute the springback error for each point in the input grid set. Springback error is determined by measuring the distance between each input grid point and its corresponding point in the output grid set. Using the method outlined in (El-Salhi et al., 2012; Gill et al., 2021; Salomon, 2006), one can determine the error assuming that a grid square g_i belongs to G_{in} and a matched grid square g_j belongs to G_{out}. The algorithm, Algorithm 1, takes as input two sets of grid points, G_{in}(the input grid points) and G_{out}(the output grid points), and produces a set E containing the springback errors for each point.

Algorithm 2: Training Set Generation.

Input: F_{in}, F_{out}, and w
Output: T (training set)
$T \leftarrow \varnothing$;
$H \leftarrow$ Heatmap generated from F_{in} ; `// See Sub-section 3.1.2`
$G_{in} \leftarrow$ Input grid generated from F_{in} using grid size $w/3$;
$G_{out} \leftarrow$ Output grid generated from F_{out} using grid size $w/3$;
foreach g_{in_i} *in* G_{in} **do**
  $s_i \leftarrow$ Calculated springback value ; `// See Sub-section 3.1.1`
  $I_i \leftarrow$ Sub-image from H for grid square g_{in_i} ; `// See Sub-section 3.1.2`
  $T \leftarrow T \cup \langle I_i, s_i \rangle$;
return T;

This pseudocode (Algorithm 2) outlines the procedure for generating a training set T used in a model that predicts springback (or some other desired output) from given input fields F_{in} and F_{out}. The algorithm starts by initializing an empty training set T. Then, a heatmap H is generated from F_{in}; this heatmap often encodes spatial or intensity-related information that will be used as part of the input features.

Next, two grids are created: G_{in} from F_{in} and G_{out} from F_{out}. Both grids use a particular granularity or cell size ($w/3$ in this example), dividing the input and output images (or fields) into smaller squares or segments. These smaller grid squares serve as the basis for localized analysis and feature extraction.

The algorithm then iterates over each grid cell g_{in} in G_{in}. For every cell, it calculates a corresponding springback value s_i, presumably by comparing the local geometry or other relevant parameters between F_{in} and G_{out}. This step references a sub-section in the text 3.1.1 that presumably contains more details on how the springback value is derived.

Simultaneously, a sub-image I_i is extracted from the heatmap H for the region defined by g_{in}. This sub-image, corresponding to the same local region as g_{in}, contains the relevant features needed for training the model—such as local curvature, gradient, intensity, or temperature distributions, depending on the application. The method for extracting or computing this sub-image is detailed in another sub-section 3.1.2.

Finally, the pair (I_i,s_i) is added to the training set T. By collecting these pairs across all grid cells, the algorithm assembles a comprehensive training set that maps localized input features (sub-images of H) to corresponding output labels (the computed springback values). At the end, the completed training set T is returned for subsequent model training or analysis.

3.2 Problem Transformation

In traditional springback error prediction methods, local geometric information is typically represented by point sequences or local geometric matrices. These methods have limitations when dealing with complex geometries and nonlinear deformations. To address these issues, we propose converting the springback error prediction problem from a geometric problem to an image processing problem.

Traditional methods often require manual feature design and struggle to fully capture geometric details. In contrast, Convolutional Neural Networks (CNNs) excel at processing high-dimensional and complex-structured data, automatically extracting multi-level features from images. This makes CNNs ideal for processing geometric data represented by heatmaps. The detailed steps for generating heatmaps were explained in Section 3.1.

To adapt to the input requirements of CNNs, we performed several preprocessing steps on the heatmaps. First, all heatmaps were resized to 342×342 pixels to ensure uniform dimensions. This resizing step was essential for maintaining consistency in the data fed into the CNN, allowing the model to process the images efficiently without discrepancies caused by varying image sizes. Next, we cropped the heatmaps according to different grid sizes (5, 10, 15, and 20), maintaining a 3×3 structure for the sub-images. For instance, with a grid size of 10, the heatmap would be divided into multiple 30×30 blocks. This method of cropping and resizing ensures that the input images are standardized in size and segmented to highlight relevant local geometrical variations, thereby enhancing the model's ability to accurately predict springback errors.

To increase the diversity of training data and improve the generalization ability of the model, we adopted various data augmentation techniques, including rotation, flipping, scaling, and translation. These data augmentation techniques generate more training samples, improving the prediction accuracy of the model in different scenarios. The preprocessed and augmented heatmaps were used as input for the CNN. ResNet extracts multi-level features through multiple convolution and pooling layers, and the fully connected layer outputs the predicted springback error. This approach leverages CNN's strengths in feature extraction, leading to more accurate and robust predictions.

3.3 Heatmap-Based Neural Framework for Springback Prediction (HNFSP)

The prediction model employed was ResNet (Residual Network) (LeCun et al., 2002). ResNet is a deep convolutional neural network. By introducing a residual structure, it effectively solves the gradient vanishing and gradient exploding problems in deep networks. This feature enables ResNet to maintain efficient training capabilities as the network depth increases and is particularly suitable for processing high-dimensional image data with complex geometric features. Compared with traditional time series models (such as LSTM and GRU), ResNet has significant advantages in processing spatial information (such as geometric changes and local feature capture).

A range of values $w/3$ was considered from $5mm$ to $20mm$, increasing in steps of $5mm$, to determine the most appropriate image/grid size for optimal performance. The advanced ResNet model consisted of N Residual blocks; N was set to 3 when the grid size was 5 mm and to 4 when the grid size was 10, 15, and 20mm. Each residual block was composed of two 3×3 convolutional layers for feature extraction and one dense (fully connected) layer with a single node for predicting springback error. An average pooling layer was included after the residual blocks to reduce spatial dimensions while retaining essential features, and the final springback error prediction is output through the fully connected layer. The residual block introduces skip connections, which enables the network to effectively transmit input information and allows gradients to be directly passed back to the previous layers. This not only reduces the difficulty of training deep networks but also enables the model to capture richer local features (such as geometric changes) and global features (such as overall shape changes). This feature is particularly important in the springback prediction problem because the local deformation and global springback characteristics of metal sheets are usually intertwined in a multi-scale manner.

Additionally, a feature fusion layer and a regression output layer were added in the custom module to better address the specific task of springback error prediction. The detailed architecture is illustrated in Figure 3. For comparison, the same shape used in the ResNet model was employed to generate a time series representation, as discussed in Section 2. This representation was used to construct three additional prediction models to be used for comparison purposes: LSTM, SVM and GRU.

The main process of the ResNet model included several steps: generating heatmaps from the point

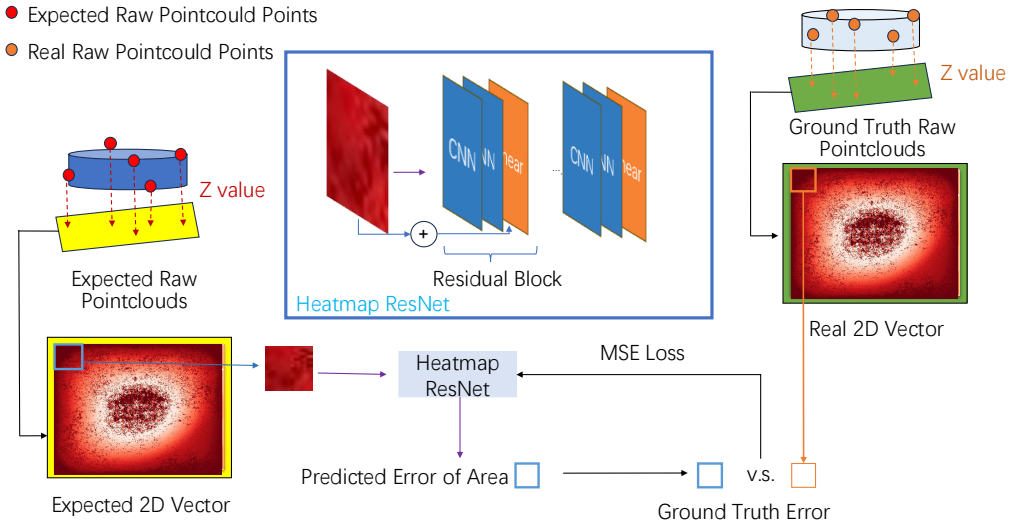

Figure 3: Heatmap-Based Neural Framework for Springback Prediction (HNFSP).

cloud and cropping the heatmaps according to the specified grid size to obtain a sub-image dataset and input it into the ResNet model. Features were extracted through multiple residual blocks, and the predicted springback error generated through a fully connected regression layer. The Mean Squared Error (MSE) loss function was used to calculate and compare the predicted error with the expected error, providing a measure of model performance and enabling comparison with the time series-based models. This approach was forward to improve prediction accuracy. It was conjectured that this was because the spatial structure of heatmap data was a natural match for the convolution operation of ResNet. The features extracted by the convolution layer could not only capture the local deformation reflected by the different color gradients in the heatmap, but could also gradually capture more advanced geometric features through multi-level convolution. For example, at a larger grid size, ResNet could more effectively capture the overall deformation trend; at a smaller grid size, its residual block can focus on the changes in local geometric details.

Compared with the time series models (LSTM, GRU), the convolution operation of ResNet could efficiently process two-dimensional heatmap data and directly extract spatial features without designing complex sequence input methods. In addition, compared with traditional SVM methods, ResNet can better handle nonlinear and high-dimensional data, so it performed better in predicting complex geometric deformations (such as springback error).

4 EXPERIMENT

4.1 Experiment Settings

For the evaluation, a titanium alloy (Ti-6Al-4V) flat-topped pyramid shape ($342 \times 342 \times 30$mm) was used, which is the standard shape for evaluating springback prediction, similar to the shapes used in (Chen et al., 2023; El-Salhi et al., 2012; El-Salhi et al., 2013; Khan et al., 2012; Khan et al., 2015). For the proposed SPIG approach, the dataset was augmented by: (i) rotating each image through 90, 180, and 270 degrees; (ii) flipping the original image; and (iii) rotating the flipped image through 90, 180, and 270 degrees, resulting in a seven-fold increase in training data size.

The experimental steps include data preprocessing, model training, and validation. First, we collected CAD (G_{in}) and actual (G_{out}) point cloud data and converted them into 342×342 heatmaps, then standardized and enhanced them. The dataset was split into training and validation sets in an 8:2 ratio. We applied data augmentation techniques such as rotation, flipping, scaling, and translation to increase data diversity. The batch size was 64, with 1000 epochs and a learning rate of $\alpha = 0.0001$. We used the Adam optimization algorithm with mean square error (MSE) as the loss function. The preprocessed data were then used to train the ResNet model, with appropriate parameters set and continuous monitoring of loss value and evaluation metrics.

Finally, the model's prediction performance was evaluated using the validation set, and the evaluation indicators recorded and analyzed to compare the per-

formance differences under different models and settings. Model performance was assessed using Mean Absolute Error (MAE), Mean Square Error (MSE), Root Mean Square Error (RMSE), and determination coefficient values (R^2).

The rest of this section is organised as follows: The point series local geometry representation, with which the proposed SPIG approach was compared, is considered in further detail in section 4.2. The two evaluation objectives are then considered in Subsections 4.4 and 4.5 respectively.

4.2 Point Series Approach

The operation of the proposed SPIG approach was compared with three-point series-based models, LSTM, SVM, and GRU. Details concerning these models were presented previously in (Chen et al., 2023). However, for completeness, a brief description of the process for generating local geometry point series representations is presented here.

As seen in Figure 4, the goal is to represent the local geometry around each $g_i \in G_{in}$ in terms of the z value difference between g_i and each of its neighbouring grid squares. A labelled point series $P = \langle P, e \rangle = \langle [p_1, p_2, \ldots, p_n], e \rangle$ was used to represent each $g_i \in G_{in}$. Here, e is the associated springback value in E, and p_j is the difference in z values between grid square g_i and its neighbour g_j. Many configurations exist for these point series, but the most straightforward is to look at each grid square in G_{in}'s eight immediate neighbours (three at corners and five at edges), as illustrated in Figure 4. As long as the point series are formed consistently, the order in which they are generated is irrelevant.

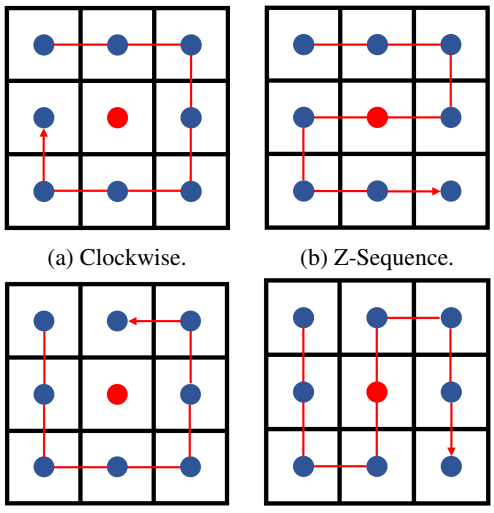

(a) Clockwise. (b) Z-Sequence. (c) Reverse. (d) N-Sequence

Figure 4: Example of point series generation.

After calculating the set of errors $\{e_1, e_2, \ldots\}$ and the set of point series $\{P_1, P_2, \ldots\}$, the errors and point series can be added to the training set $D_{train} = \{T_1, T_2, \ldots\}$, where each $T_i = \langle P_i, e_i \rangle$.

4.3 Experiment Result

The evaluation results are presented in Table 1. From the table it can be seen that the ResNet model performs better than LSTM, GRU, and SVM models with respect to all metrics (MAE, MSE, RMSE, and R2) for all grid sizes (5mm, 10mm, 15mm, and 20mm). ResNet provides the greatest benefit at bigger grid sizes, and prediction accuracy typically increases with grid size. For instance, ResNet outperforms GRU (0.2566), LSTM (0.3067), and SVM (0.4569) with an MAE of 0.1909 at a 5mm grid size. ResNet has a mean square error (MSE) of 0.0258, whereas GRU, LSTM, and SVM have MSEs of 0.1747, 0.1640, and 0.1452, respectively, with a grid size of 20 mm. Furthermore, ResNet continuously obtains the greatest R2 values (e.g., 0.9688 at 10 mm), demonstrating its better neural design for capturing spatial data.whereas SVM is computationally efficient, it suffers from the nonlinear, high-dimensional nature of spatial feature extraction, whereas LSTM and GRU, which are mainly intended for sequential data, are less effective at this task. Consequently, across all grid sizes, ResNet has the highest springback error prediction accuracy and stability.

Table 1: TCV evaluation results, in tabular format, obtained using four different models and a range image/grid sizes (Grid size $(w/3) = \{5, 10, 15, 20\}$).

Grid Size	Method	Metrics			
		MAE	MSE	RMSE	R2
5 mm	LSTM(Bingqian et al., 2024)	0.3067	0.1580	0.3963	0.9140
	SVM(Bingqian et al., 2024)	0.4569	0.3637	0.6005	0.8036
	GRU(Chen et al., 2023)	0.2566	0.1544	0.3930	**0.9228**
	ResNet	**0.1909**	**0.1094**	**0.3307**	0.9221
10 mm	LSTM(Bingqian et al., 2024)	0.3002	0.1596	0.3981	0.8921
	SVM(Bingqian et al., 2024)	0.3592	0.2206	0.4688	0.8518
	GRU(Chen et al., 2023)	0.2573	0.1476	0.3842	0.9123
	ResNet	**0.1216**	**0.0334**	**0.1830**	**0.9688**
15 mm	LSTM(Bingqian et al., 2024)	0.3129	0.1664	0.4071	0.8750
	SVM(Bingqian et al., 2024)	0.3239	0.1784	0.4215	0.8668
	GRU(Chen et al., 2023)	0.2613	0.1455	0.3814	0.9015
	ResNet	**0.1151**	**0.0332**	**0.1822**	**0.9498**
20 mm	LSTM(Bingqian et al., 2024)	0.3028	0.1640	0.4043	0.8751
	SVM(Bingqian et al., 2024)	0.2925	0.1452	0.3796	0.8899
	GRU(Chen et al., 2023)	0.2957	0.1747	0.4179	0.8609
	ResNet	**0.1158**	**0.0258**	**0.1608**	**0.9537**

4.4 Comparison with Point Series Approach

We conducted additional experiments to compare the proposed ResNet architecture with a GRU-based model across multiple grid sizes (5 mm, 10 mm, 15 mm, and 20 mm), as summarized in Table 2.

Table 2: Performance comparison of GRU and ResNet across multiple grid sizes (Grid size $(w/3) = \{5, 10, 15, 20\}$) in terms of parameters, FLOPs, and training time.

Method	Parameters (K)	FLOPs (M)	Grid Size	Training Time (minutes)
GRU(Chen et al., 2023)	103	31.5	5 mm	16.3
			10 mm	24.3
			15 mm	25.2
			20 mm	21.1
ResNet	308	133	5 mm	**7.2**
			10 mm	**3.2**
			15 mm	**2.0**
			20 mm	**1.5**

Table 2 presents a comparison of the training times that were recorded. From the table it can seen that ResNet achieves significantly shorter training times across all grid sizes than GRU. For instance, at a 10 mm grid size, ResNet requires only 3.2 minutes for training, while GRU takes 24.3 minutes. This efficiency is consistent across grid sizes, with ResNet being approximately 4-8 times faster. Despite having a larger parameter count (308K vs. 103K) and higher FLOPs (133M vs. 31.5M), ResNet's parallel convolutional operations make it better suited for heatmap data, reducing computational overhead significantly.

In contrast, despite its smaller parameter size and lower FLOPs, GRU's sequential processing leads to inefficiencies. These findings highlight ResNet's superior computational efficiency and scalability, making it more effective for tasks involving heatmap representations and larger datasets.

In summary, the ResNet model significantly outperforms LSTM, SVM, and GRU models in predicting springback error, especially in terms of accuracy and stability. Thus, the ResNet model is the preferred choice for similar springback error prediction tasks.

4.5 Best Grid/Image Size

Inspection of Table 1with regard to the range of grid sizes considered reveals that grid size has a significant impact on prediction accuracy. As the grid size increases from 5mm to 20mm, the prediction error of the ResNet model decreases, and the R2 value improves, indicating better capture of springback characteristics. Specifically, with a 20mm grid size, the ResNet model achieves the lowest MAE of 0.1158, MSE of 0.0258, RMSE of 0.1608, and R2 of 0.9537, demonstrating the best performance. Improved performance with larger grid sizes highlights the model's enhanced ability to capture intricate geometric details, thereby improving prediction accuracy. These results emphasize the importance of selecting appropriate grid sizes for accurate predictions and demonstrate the ResNet model's robustness and adaptability. The ResNet model consistently outperforms others, showcasing its capability to leverage detailed geometric information from various grid sizes for high-precision predictions.

In summary, for springback error prediction, the ResNet model performs best with a grid size of 20 mm. Therefore, choosing a larger grid size (such as 20mm) as the division standard for input data can more effectively improve the prediction accuracy and stability of the model. This finding has important guiding significance for parameter selection in practical applications.

5 CONCLUSION

The Springback Prediction Using Image Geometires (SPIG) approach for predicting the springback associated with cold incremental sheet forming has been proposed. By converting local geometric information into two-dimensional heatmaps and processing these heatmaps using a few residual blocks, we achieve high-precision prediction of springback error. Experimental results show that the ResNet model performs best under all grid sizes (5mm, 10mm, 15mm, and 20mm), especially in terms of MSE and RMSE, significantly better than the LSTM, SVM, and GRU models. This proves the superior performance of the ResNet model in springback error prediction and demonstrates its powerful ability to capture geometric features.

By comparing different grid sizes, it was found that a larger grid size (such as 20 mm) can more effectively capture the characteristics of springback error, thereby improving the model's prediction accuracy. Compared with traditional methods, the ResNet model shows higher accuracy and stability when dealing with springback error prediction problems. Therefore, choosing an appropriate grid size and fully utilizing the advantages of ResNet are key to improving springback error prediction accuracy.

Future research can optimize the model structure, explore additional data augmentation techniques, combine multi-modal data (such as material properties and processing parameters), and investigate real-time prediction and feedback control systems. This method will also be extended to other complex moulding processes (such as hot forming and composite material moulding) to verify its versatility. These efforts will enhance the accuracy of springback error prediction and advance intelligent manufacturing technology, providing more efficient solutions for industrial production.

REFERENCES

Bahloul, R., Arfa, H., and Salah, H. B. (2013). Application of response surface analysis and genetic algorithm for the optimization of single point incremental forming process. *Key Engineering Materials*, 554:1265–1272.

Belytschko, T. and Hodge Jr, P. G. (1970). Plane stress limit analysis by finite elements. *Journal of the Engineering Mechanics Division*, 96(6):931–944.

Bingqian, Y., Zeng, Y., Yang, H., Oscoz, M. P., Ortiz, M., Coenen, F., and Nguyen, A. (2024). Springback prediction using point series and deep learning. *The International Journal of Advanced Manufacturing Technology*, 132(9):4723–4735.

Boser, B. E., Guyon, I. M., and Vapnik, V. N. (1992). A training algorithm for optimal margin classifiers. In *Proceedings of the fifth annual workshop on Computational learning theory*, pages 144–152.

Canny, J. (2009). A computational approach to edge detection. *IEEE Transactions on pattern analysis and machine intelligence*, (6):679–698.

Chen, D., Coenen, F., Hai, Y., Oscoz, M. P., and Nguyen, A. (2023). Springback prediction using gated recurrent unit and data augmentation. In *International Conference on Mechatronics and Intelligent Robotics*, pages 1–13. Springer.

Duda, R. O. and Hart, P. E. (1972). Use of the hough transformation to detect lines and curves in pictures. *Communications of the ACM*, 15(1):11–15.

El-Salhi, S., Coenen, F., Dixon, C., and Khan, M. S. (2012). Identification of correlations between 3d surfaces using data mining techniques: Predicting springback in sheet metal forming. In *International Conference on Innovative Techniques and Applications of Artificial Intelligence*, pages 391–404. Springer.

El-Salhi, S., Coenen, F., Dixon, C., and Khan, M. S. (2013). Predicting features in complex 3d surfaces using a point series representation: a case study in sheet metal forming. In *International Conference on Advanced Data Mining and Applications*, pages 505–516. Springer.

Fix, E. (1985). *Discriminatory analysis: nonparametric discrimination, consistency properties*, volume 1. USAF school of Aviation Medicine.

Gill, P. E., Murray, W., and Wright, M. H. (2021). *Numerical linear algebra and optimization*. SIAM.

Goodfellow, I. J., Pouget-Abadie, J., Mirza, M., Xu, B., Warde-Farley, D., Ozair, S., Courville, A., and Bengio, Y. (2014). Generative adversarial nets. *Advances in neural information processing systems*, 27.

Harris, C., Stephens, M., et al. (1988). A combined corner and edge detector. In *Alvey vision conference*, volume 15, pages 10–5244. Manchester, UK.

He, J., Cu, S., Xia, H., Sun, Y., Xiao, W., and Ren, Y. (2025). High accuracy roll forming springback prediction model of svr based on sa-pso optimization. *Journal of Intelligent Manufacturing*, 36(1):167–183.

He, K., Zhang, X., Ren, S., and Sun, J. (2016). Deep residual learning for image recognition. In *Proceedings of the IEEE conference on computer vision and pattern recognition*, pages 770–778.

Holland, J. H. (1975). An introductory analysis with applications to biology, control, and artificial intelligence. *Adaptation in Natural and Artificial Systems. First Edition, The University of Michigan, USA*.

Khan, M. S., Coenen, F., Dixon, C., and El-Salhi, S. (2012). Classification based 3-d surface analysis: predicting springback in sheet metal forming. *Journal of Theoretical and Applied Computer Science*, 6(2):45–59.

Khan, M. S., Coenen, F., Dixon, C., El-Salhi, S., Penalva, M., and Rivero, A. (2015). An intelligent process model: predicting springback in single point incremental forming. *The International Journal of Advanced Manufacturing Technology*, 76(9):2071–2082.

Kingma, D. P., Welling, M., et al. (2013). Auto-encoding variational bayes.

LeCun, Y., Bottou, L., Bengio, Y., and Haffner, P. (2002). Gradient-based learning applied to document recognition. *Proceedings of the IEEE*, 86(11):2278–2324.

Loh, W.-Y. (2011). Classification and regression trees. *Wiley interdisciplinary reviews: data mining and knowledge discovery*, 1(1):14–23.

Lowe, D. G. (2004). Distinctive image features from scale-invariant keypoints. *International journal of computer vision*, 60(2):91–110.

Maji, K. and Kumar, G. (2020). Inverse analysis and multi-objective optimization of single-point incremental forming of aa5083 aluminum alloy sheet. *Soft Computing*, 24(6):4505–4521.

Martins, P., Bay, N., Skjødt, M., and Silva, M. (2008). Theory of single point incremental forming. *CIRP annals*, 57(1):247–252.

Sakoe, H. and Chiba, S. (2003). Dynamic programming algorithm optimization for spoken word recognition. *IEEE transactions on acoustics, speech, and signal processing*, 26(1):43–49.

Salomon, D. (2006). *Curves and surfaces for computer graphics*. Springer.

Sbayti, M., Bahloul, R., and Belhadjsalah, H. (2020). Efficiency of optimization algorithms on the adjustment of process parameters for geometric accuracy enhancement of denture plate in single point incremental sheet forming. *Neural Computing and Applications*, 32(13):8829–8846.

Seeger, M. (2004). Gaussian processes for machine learning. *International journal of neural systems*, 14(02):69–106.

Seo, K.-Y., Kim, J.-H., Lee, H.-S., Kim, J. H., and Kim, B.-M. (2017). Effect of constitutive equations on springback prediction accuracy in the trip1180 cold stamping. *Metals*, 8(1):18.

Serra, J. (1983). *Image analysis and mathematical morphology*. Academic Press, Inc.

Spathopoulos, S. C. and Stavroulakis, G. E. (2020). Springback prediction in sheet metal forming, based on finite element analysis and artificial neural network approach. *Applied Mechanics*, 1(2):97–110.

Tranmer, M. and Elliot, M. (2008). Multiple linear regression. the cathie marsh centre for census and survey research(ccsr), 5 (5), 1-5.

Zajkani, A. and Hajbarati, H. (2017). An analytical modeling for springback prediction during u-bending process of advanced high-strength steels based on anisotropic nonlinear kinematic hardening model. *The International Journal of Advanced Manufacturing Technology*, 90(1):349–359.

Zeng, D. and Xia, Z. C. (2005). An anisotropic hardening model for springback prediction. In *AIP Conference Proceedings*, volume 778, pages 241–246. American Institute of Physics.

Zwierzycki, M., Nicholas, P., and Ramsgaard Thomsen, M. (2017). Localised and learnt applications of machine learning for robotic incremental sheet forming. In *Humanizing digital reality: Design modelling symposium Paris 2017*, pages 373–382. Springer.